Rock Mech Rock Eng (2014) 47:1849–1865
DOI 10.1007/s00603-013-0495-3

ORIGINAL PAPER

Crack Initiation and Crack Propagation in Heterogeneous Sulfate-Rich Clay Rocks

Florian Amann · Ömer Ündül · Peter K. Kaiser

Received: 15 January 2013 / Accepted: 11 October 2013 / Published online: 24 October 2013

Abstract Brittle fracture processes were hypothesized by several researches to cause a damage zone around an underground excavation in sulfate-rich clay rock when the stress exceeds the crack initiation threshold, and may promote swelling by crystal growth in newly formed fractures. In this study, laboratory experiments such as unconfined and confined compression tests with acoustic emission monitoring, and microstructural and mineralogical analyses are used to explain brittle fracture processes in sulfate-rich clay rock from the Gipskeuper formation in Switzerland. This rock type typically shows a heterogeneous rock fabric consisting of distinct clayey layers and stiff heterogeneities such as anhydrite layers, veins or nodules. The study showed that at low deviatoric stress, the failure behavior is dominated by the strength of the clayey matrix where microcracks are initiated. With increasing deviatoric stress or strain, growing microcracks eventually are arrested at anhydrite veins, and cracks develop either aligned with the interface between clayey layers and anhydrite veins, or penetrate anhydrite veins. These cracks often link micro-fractured regions in the specimen. This study also suggest that fracture localization in sulfate-rich clay rocks, which typically show a heterogeneous rock fabric, does not take place in the pre-peak range and renders unstable crack propagation less likely. Sulfate-rich clay rocks typically contain anhydrite veins at various scales. At the scale of a tunnel, anhydrite layers or veins may arrest growing fractures and prevent the disintegration of the rock mass. The rock mass may be damaged when the threshold stress for microcrack initiation is exceeded, thus promoting swelling by crystal growth in extension fractures, but the self-supporting capacity of the rock mass may be maintained rendering the possibility for rapidly propagating instability less likely.

Keywords Crack initiation · Crack propagation · Brittle failure · Heterogeneous rock · Sulfate-rich clay rock · Gipskeuper

1 Introduction

Sulfate-rich clay rocks of the Keuper formation in Switzerland and south-west Germany are among the most difficult rock types to characterize in terms of their rock mechanical and engineering geological properties, and their failure behavior. The difficulties in characterization are to a considerable extent related to the anisotropy, the heterogeneity and often the intense folding at various scales. Beside these characterization issues, several tunnels through these sulfate-rich clay rocks encountered severe and costly problems during construction and operation. These problems are mostly associated with gypsum precipitation from a supersaturated sulfate solution (Alonso and Berdugo 2006; Vögtli and Jordan 1996) in pre-existing tectonic structures or fissure which were created and

F. Amann (✉)
Engineering Geology, Institute of Geology,
Swiss Federal Institute of Technology, Zurich,
Sonneggstrasse 5, 8092 Zurich, Switzerland
e-mail: florian.amann@erdw.ethz.ch

Ö. Ündül
Geological Engineering Department, Engineering Faculty,
Istanbul University, Avcilar, 34320 Istanbul, Turkey
e-mail: oundul@istanbul.edu.tr

P. K. Kaiser
Center for Excellence in Mining Innovation,
936 Ramsey Lake Road, Sudbury P3E 6H5, Canada
e-mail: pkaiser@miningexcellence.ca

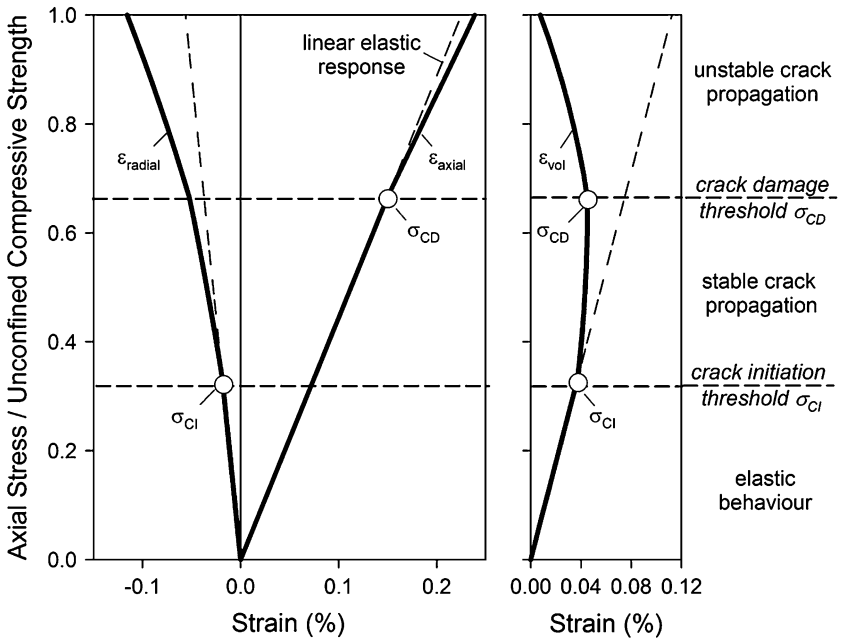

Fig. 1 Stress thresholds of a brittle failing rock under unconfined compression (according to Brace et al. 1966; Hallbauer et al. 1973; Scholz 1968; Martin and Chandler 1994; Fairhurst and Cook 1966; Bieniawski 1967; Lajtai 1974; Tapponier and Brace 1976; Martin 1997)

opened as a consequence of stress redistribution (Alonso and Berdugo 2006), causing volume expansion and invert heaves of up to several decimeters within weeks or months after tunnel excavation (Amstad and Kovari 2001; Steiner 1993).

Kaiser and Kim (2008), Amann et al. (2010) and Steiner et al. (2010, 2011) hypothesized that excavation-induced brittle fracturing in sulfate-rich clay rock types may contribute to the creation of preferential flow path for supersaturated groundwater in the tunnel near-field, thus promoting swelling by crystal growth in extension fractures. The hypothesis of brittle fracture formation in this rock type is based on research on fracture processes in hard crystalline and sedimentary rock types under compressive load on both, the laboratory and the tunnel scale. Compression tests on cylindrical specimen showed that brittle rocks fail as a consequence of microcrack initiation, propagation and eventually coalescence when a critical microcrack density is approached (Lockner et al. 1992). Under unconfined compressive loads, extensional microcracks are initiated at an axial stress of approximately 0.3–0.6 of the unconfined compressive strength UCS (Fig. 1; after Brace et al. 1966; Hallbauer et al. 1973; Scholz 1968; Martin and Chandler 1994; Fairhurst and Cook 1966; Bieniawski 1967; Lajtai 1974; Tapponier and Brace 1976; Martin 1997). These microcracks are initially predominantly aligned with the maximum principal stress orientation. Crack initiation at σ_{CI} is accompanied by dilatancy, and thus the volumetric strain curve deviates from linearity (Fig. 1). At this stage of brittle failure, the microcracks grow in a stable manner (Bieniawski 1967). With increasing stress or strain, accumulation of microcracks eventually leads to a volumetric strain reversal (Fig. 1) which is typically between 0.7 and 0.9 times the peak strength (Martin 1997). The volumetric reversal point is also called the crack damage threshold and defines the onset of unstable crack growth (Bieniawski 1967). With further increase in axial load, microcracks accumulate, reach a critical crack density, and the specimen ultimately fails by splitting or kinkband-type shear failure at higher confinement.

Brittle failure processes in sulfate-rich clay rocks were not studied in detail so far, and the hypothesis of brittle fracturing as well as the stress magnitudes required to initiate microcracks in sulfate-rich clay rocks is not yet investigated. This experimental study was initiated to investigate the failure behavior of sulfate-rich clay rock under confined and unconfined compression. The study is primarily focused on identifying the stress magnitude at which microcracks initiate, and the influence of factors such as mineralogical composition and heterogeneities that affect both fracture propagation and strength.

2 Sampling and Testing Methods

2.1 Sampling, Specimen Handling and Specimen Preparation

The samples for this study were extracted from six boreholes drilled at the Belchen Drainage Tunnel in Switzerland in October 2011 (Fig. 2). The 84-mm-diameter cores were drilled with compressed air cooling to obtain high-quality specimens for mechanical laboratory tests. All

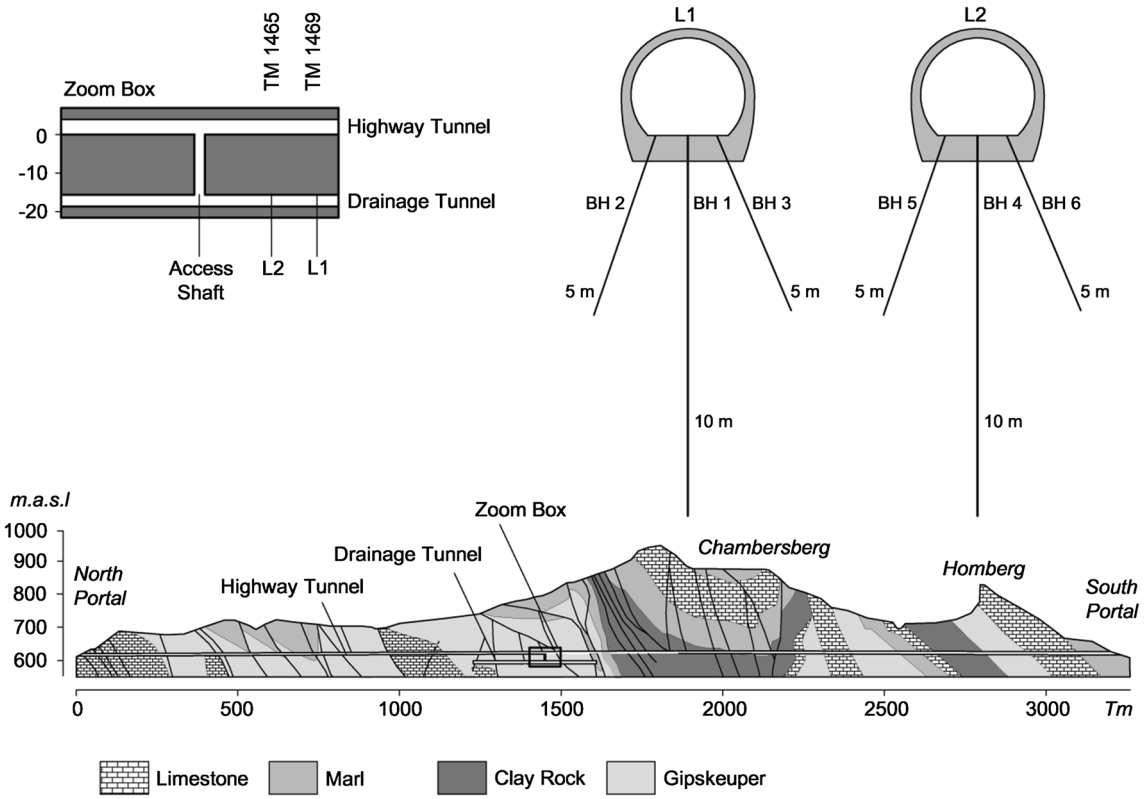

Fig. 2 Simplified geological cross section along the Belchen Highway Tunnel showing the location of boreholes (BH) drilled to extract samples for this investigation

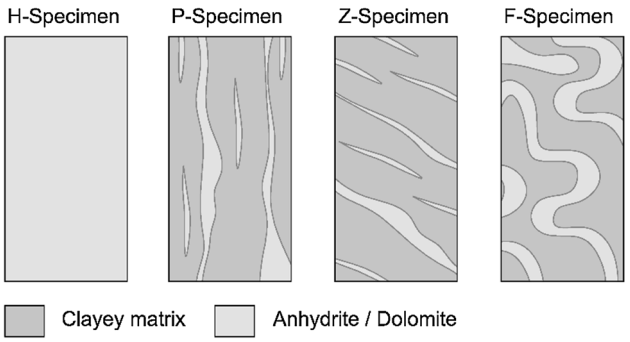

Fig. 3 Specimen geometries and nomenclature utilized to categorize specimens for unconfined and confined compression tests

cores taken from double-tube core barrels were hermetically sealed in vacuum-evacuated foil immediately after core extraction and core description. These sealed cores were stored in core boxes and protected against dynamic perturbation during transport utilizing air pillows and foam.

The Gipskeuper formation is characterized by an extensive heterogeneity, folding, and physical anisotropy at multiple scales (e.g., mm to m scale). Therefore, cores taken from boreholes in this geological formation show various bedding plane orientations and mineralogical compositions. The mineralogical composition encountered in the cores of the six boreholes (Fig. 2) spans from almost pure anhydrite/dolomite sections (clay content <5 %) to clay rock sections with clay content up to 50 %. Depending on the mineralogical composition and the orientation of the load axis with respect to the bedding plane or vein/layer orientation, rock mechanical properties may vary widely. Therefore, 34-mm cores were extracted by over-coring (perpendicular) of the 84-mm-diameter cores under dry conditions to obtain four specimen geometries (Fig. 3):

1. H-Specimens: specimens with a homogeneous rock fabric without distinct clay layers
2. P-specimens: the load axis is oriented approximately parallel to the bedding orientation or the orientation of veins or layers (e.g., within ±5°–10°).
3. Z-specimens: the loading axis is oriented approximately 35°–55° with respect to the bedding plane orientation or the orientation of veins or layers; and
4. F-specimens: specimens where bedding planes, veins or layers are folded. For this specimen type, the load axis has various orientations with respect to the rock fabric.

Note that at the specimen scale, heterogeneities can be continuous (layers) or discontinuous (veins). For unconfined compressive strength, test specimens were selected as

to investigate mechanical properties and behavior for the range of rock fabric and mineralogical composition encountered in the boreholes. Almost pure anhydrite/dolomite specimens with a macroscopic homogeneous rock fabric and specimens with high content of clay and heterogeneous rock fabric were considered as end-members for the strength and failure behavior. Specimen selection for confined compressive strength tests was based on core logging and limited to heterogeneous rock fabric (e.g., specimens with distinct layers of clay rock and stiff heterogeneities).

Rock mechanical properties may degrade at shallow depth below the tunnel invert due to unloading, swelling or slaking. Thus, only specimens taken from a depth >2.5 m below the tunnel invert were used for mechanical testing. For the unconfined tests, two specimen diameters were utilized: 84 and 34 mm. For confined tests, only 34-mm-diameter specimens were used. All specimens were cut under dry conditions at the Institute of Geotechnical Engineering at the Swiss Federal Institute of Technology in Zurich using a rigid prismatic specimen holder and an electronically controlled diamond-saw Type DRAMET BS 270. The constant band rotating speed (1,200 m/min), the constant feed rate (4 mm/min) and the thin metal band (0.7 mm) populated with diamonds at both sides of the cutting edge allows for vibrationless cutting and polishing. After cutting, the parallelism of the end faces met the requirements of the ISRM suggested methods (1979). The environmental exposure time of the specimens was minimized through a rigorous preparation procedure and immediate sealing of the specimens between subsequent preparation steps.

2.2 Mineralogical Analyses

Mineralogy of the specimens was determined on randomly oriented powder specimens with X-ray diffraction (XRD) analysis. The samples were crushed with a jaw breaker <0.4 mm and homogenized. X-ray diffraction measurements were made using a Bragg–Brentano diffractometer (Philips PW1820). The powder samples were step-scanned at room temperature from 2 to 75°2Theta (step width 0.02°2Theta, counting time 4 s). The qualitative phase composition was determined with the software DIFFRACplus (BRUKER AXS). The mineral composition of the samples was determined with the Rietveld program AutoQuan (GE SEIFERT).

2.3 Thin Section Analyses

Thin sections for this study were prepared from selected specimens either before or after mechanical testing. Prior to thin section preparation, a highly viscous, blue-stained epoxy resin was drawn into the samples under a moderate vacuum. This resin penetrates cracks in the samples and allows for a better identification of cracks under the microscope. All thin sections were prepared under dry conditions.

2.4 Unconfined Compressive Strength Testing Procedure

Unconfined compressive strength tests were performed at the rock mechanical laboratory at the Chair of Engineering Geology at the Swiss Federal Institute of Technology in Zurich. A modified 2,000 kN Walter and Bai servo-hydraulic rock testing device with digital feedback control was utilized. Axial and circumferential strain gages were mounted onto the specimen at half of the specimen height to eliminate the influence of end effects on the strain measurements. Two axial strain gages (Type BD 25/50, DD1) were firmly attached to opposite sides of the specimens. The base length was 50 mm for the 84-mm-diameter specimens and 35 mm for the 34-mm-diameter specimens. The radial strain (ε_{rad}) was calculated from the displacement measured by a single gage (Type 3544-150 M-120 m-ST) attached to a chain wrapped tightly around the specimen.

The failure of unconfined or slightly confined brittle solids is commonly associated with the development of axial cracks, and the circumferential displacement as a function of axial load tends to increase disproportionately compared to the axial displacement curve. Thus, for unconfined compression tests in this study, the circumferential displacement rate was utilized as the feedback signal for controlling the load throughout the failure of the specimen. The axial load was increased in such a way to give a constant circumferential displacement rate of 0.05 mm/min. Before testing of the rock specimens, all strain gages and the load cells were calibrated.

2.5 Triaxial Testing Procedure

Confined compressive strength tests were performed at the Rock Mechanics Laboratory at the Swiss Federal Institute of Technology in Lausanne. A 2,000 kN Walter and Bai servo-hydraulic rock testing device with digital feedback control was used. The axial displacement was measured with 20-mm HBM LVDT. The axial displacement was used as the controlling feedback signal. The selected rate was 0.001 mm/s. During the test, the volume loss or gain in the Hoek cell was continuously measured with an accuracy of 0.1 cm^3. The oil-volume changes were utilized to calculate the volumetric strain ($\varepsilon_{vol,oil}$) of the specimen assuming a cylindrical deformation of the specimen.

For this study, four confining stress levels were utilized: 1, 2, 4 and 8 MPa. Prior to deviatoric loading, the axial load and the confining stress were increased simultaneously to establish the pre-defined hydrostatic stress conditions. Deviatoric loading was applied by increasing the axial load as the confining stress was kept constant.

2.6 Determination of the Onset of Dilatancy

The onset of dilation in brittle rocks is often associated with micro-cracking and a disproportional increase of the lateral strain with respect to the axial strain. Different methodologies have been developed since the 1960s to establish the onset of dilation based on the stress–strain response or micro-acoustic activity (Brace et al. 1966; Bieniawski 1967; Lajtai 1974; Martin and Chandler 1994; Eberhardt et al. 1998; Nicksiar and Martin 2012).

For the unconfined compression tests performed in this study, two strain-based methods were utilized, which have been shown to give accurate estimates of the onset of dilatancy (Nicksiar and Martin 2012; Amann et al. 2011a). The two different strain-based approaches are illustrated in Fig. 4a and b.

Method I: Brace et al. (1966) suggested that the onset of dilation can be established by examining when the stress–volumetric strain curve deviates from its linear portion at low axial stress (Fig. 4a). Volumetric strain (ε_{vol}) was calculated from the sum of the arithmetic mean of the two axial strains (ε_{axial}) and two times the radial strain ($\varepsilon_{axial} + 2\varepsilon_{radial}$).

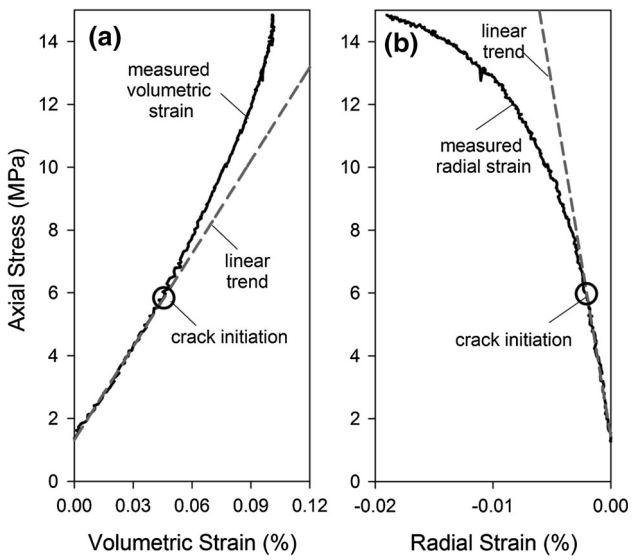

Fig. 4 Methodology for determining the crack initiation threshold in unconfined compression tests by examining **a** the volumetric strain response according to Brace et al. (1966) and **b** the radial strain response according to Lajtai (1974). The *dashed lines* represent the linear trend

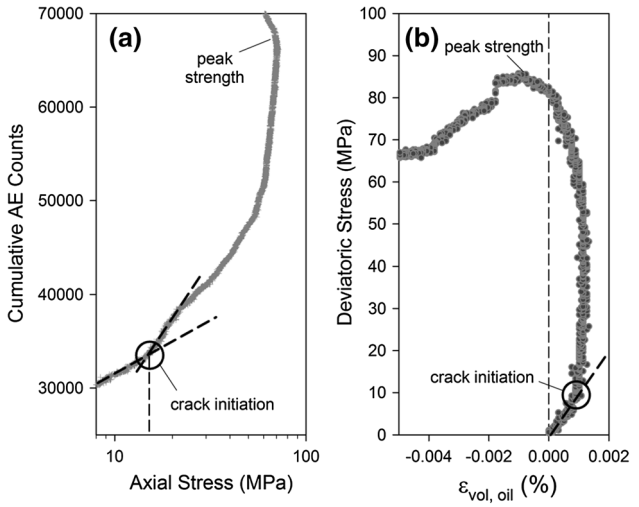

Fig. 5 Methodology for determining the crack initiation threshold in confined compression tests by examining **a** acoustic emission data according to Eberhardt et al. (1998), and **b** the volumetric strain response obtained from oil-volume gain or loss in the Hoek cell during deviatoric loading. The *dashed line* in **b** represents the linear trend at low deviatoric stress

Method II: Lajtai (1974) applied the same principles as Brace et al. (1966) to the radial strain curve. The onset of dilatancy is taken at the point where the stress–radial strain curve deviates from linearity (Fig. 4b).

In confined compressive strength tests, the micro-acoustic activity was examined to establish the onset of micro-cracking as suggested by Eberhardt et al. (1998) and illustrated in Fig. 5a. A Euro Physical Acoustics AE-system was utilized. Two 17-mm diameter broad-band piezoelectric sensors (Type Euro Physical Acoustics WSa) with the sensitivity between 10 and 1,000 kHz were firmly affixed on the triaxial cell. Amplification was achieved in two stages: The first was a pre-amplifier stage with a 30-dB gain. Before the signal enters the transient recorder, a second stage of amplification was applied with a 40-dB gain. Recording of the data was triggered when the signal amplitude exceeded a pre-defined amplitude threshold.

In addition to the micro-acoustic activity, the oil-volume gain and loss from the Hoek cell during deviatoric loading was used to define the onset of dilation according to the method suggested by Brace et al. (1966) (Fig. 5b). It was assumed that, due to the short-test duration, temperature variations in the laboratory do not have a significant effect on the volume strain. The data show considerable scatter (Fig. 5b). Thus, only test results with a high signal-to-noise ratio were analyzed.

Table 1 Results from unconfined compressive strength tests

Borehole	Depth (cm)	Specimen	D (mm)	E (GPa)	υ	UCS (MPa)	σ_{CI} (I) (MPa)	σ_{CI} (II) (MPa)
B3	330	Z	34	2.8	0.13	5.6	4.0	3.8
B4	287	P	34	5.2	0.08	6.6	4.0	4.4
B4	630	Z	84	4.9	0.09	7.7	4.0	3.8
B3	335	Z	34	6.4	0.17	7.8	4.6	4.2
B3	318	F	34	6.1	0.09	11.9	6.6	6.4
B3	270	F	84	9.4	0.04	16.1	6.5	6.5
B3	445	P	34	42.2	0.16	20.1	15.2	12.9
B1	687	P	34	12.4	0.06	23.5	7.9	8.1
B1	385	F	34	29.7	0.19	25.5	12.4	12.1
B1	505	F	34	33.1	0.21	28	9.9	9.2
B5	485	P	84	35.3	0.07	32.6	10.5	7.7
B4	257	F	34	26.1	0.09	41.2	13.7	13.7
B3	412	P	34	65	0.18	44.6	22.1	22.4
B3	420	P	34	80.7	0	46.8	–	–
B1	495	F	34	36.1	0.11	52.6	17.4	13.4
B4	250	F	34	32.4	0.06	64.2	19.5	19.7
B3	450	P	34	68.8	0.16	71.7	45.5	40.0
B1	795	H[a]	34	84.3	0.21	75.4	63.5	61.0
B1	810	H[a]	34	77	0.21	83	72.5	63.5
B1	710	H[a]	34	85.7	0.2	93.6	67.5	55.0
B1	720	H[a]	34	80.2	0.21	150.9	89.5	85.5

Z Z-specimen, *P* P-specimen, *F* F-specimen, *H* specimen with a macroscopic homogeneous rock fabric, *D* specimen diameter, *E* Young's modulus, υ Poisson's value, *UCS* unconfined compressive strength, σ_{CI} *(I)* crack initiation determined according to Brace et al. (1966), σ_{CI} *(II)* crack initiation determined according to Lajtai (1974)

[a] H specimens with a homogeneous rock fabric without distinct clay layers

3 Results and Interpretation

3.1 Unconfined Compressive Strength Tests

3.1.1 Unconfined Compressive Strength and Crack Initiation Stress

The results for unconfined compressive strength values (UCS), elastic properties (Young's modulus E and Poisson's value υ), and the axial stress at the onset of dilation (e.g., crack initiation threshold σ_{CI}) are summarized in Table 1. Table 2 summarizes the results of the XRD analyses obtained from the specimens. The unconfined compressive strength ranges from 5.6 to 151 MPa. Values at the lower strength limit were obtained from specimens that failed through the clay matrix. The upper strength limit was obtained from H-specimens containing up to 84 % of anhydrite, and a macroscopically homogeneous rock fabric. The Young's modulus taken from the axial strain curves at low axial stresses (e.g., axial stresses below σ_{CI}) ranges from 2.8 to 85.7 GPa. The Poisson's ratios taken from the radial strain curve at low axial stresses range from 0.06 to 0.21. Figure 6 shows the relationship between UCS and σ_{CI}. For the range of unconfined compressive strength values between 5.6 and 65 MPa, σ_{CI} increases with increasing UCS at a rate of about 3:10 (trend line is shown in Fig. 6). In this range of UCS, the axial stress at crack initiation varies between 4 and 13 MPa. In the range of UCS between 65 and 75 MPa, the crack initiation stress σ_{CI} increases substantially, and beyond this UCS range (H-specimens) σ_{CI} seems to again increase at a rate of 3:10 (even though data are limited in this range; dashed trend line is shown in Fig. 6).

3.1.2 Relationship between Mineralogical Composition and σ_{CI} and UCS

The mineralogical analyses presented in Table 2 show that the mineralogical composition of the test specimens is dominated by the mass fractions of anhydrite, dolomite and clay minerals (i.e., the sum of the mass fractions of smectite, illite, and chloride). With decreasing clay content, the content of anhydrite and/or Dolomite increases. The latter minerals typically form discrete layers, veins or nodules on the mm- to cm-scale in the clayey matrix. Changing mass fractions of clay minerals are related to the total amount of anhydrite or Dolomite in the specimen and

Table 2 Results obtained from XRD analyses on specimens used for unconfined compressive strength tests

Borehole	Depth (cm)	Ah (%)	Gy (%)	Ba (%)	Do (%)	Q (%)	Mg (%)	CM (%)
B3	330	49.17	0.15	0	0	4.23	9.68	28.72
B4	287	20.28	0.63	0.22	0.68	3.49	15.91	46.23
B4	630	35.07	7.77	0	1.29	5.78	9.38	30.75
B3	335	37.76	0.86	1.15	0	5.15	14.65	25.07
B3	318	51.29	0.83	1.37	0	10.23	8.59	17.85
B3	270	57.4	0.52	1.71	0	5.2	7.73	16.54
B3	445	36.86	0.64	1.75	0.69	2.85	8.82	39.74
B1	687	30.62	4.11	0.17	0.2	9.08	25.58	20.69
B1	385	53.89	1.05	1.36	0	6.96	10.21	16.98
B1	505	65.3	0	0.16	0	1.8	19.6	8.58
B5	485	45.91	1.59	0.94	0.39	5.31	18.98	16.07
B4	257	58.94	0.44	1.32	0	6.13	14.55	10.76
B3	412	47.94	0.91	0.91	0	7.15	25.81	8.57
B3	420	–	–	–	–	–	–	–
B1	495	69.3	0	1.78	0	2.03	11.56	9.31
B4	250	70.49	0.22	1.57	0	3.57	10.89	7.24
B3	450	67.61	0.36	1.36	0	2.3	14.28	9.52
B1	795	46.35	0.52	2.13	43.87	1.31	0.05	4.4
B1	810	57.38	0.52	1.66	30.19	1.41	0.07	3.69
B1	710	80.41	0.16	1.8	12.29	0.48	0.13	2.87
B1	720	84.23	0.36	1.91	7.84	0.26	0.12	2.97

Ah anhydrite, *Gy* gypsum, *Ba* bassanite, *Do* dolomite, *Q* quartz, *Mg* magnesite, *CM* clay minerals (e.g., sum of smectite, illite, chlorite)

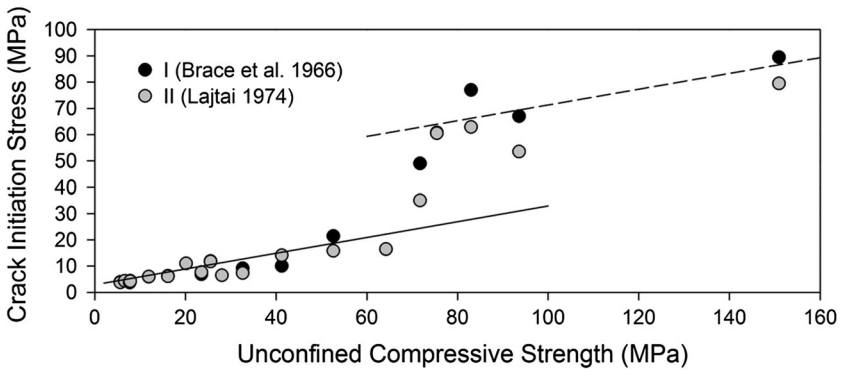

Fig. 6 Unconfined compressive strength in relation to the axial stress at the onset of dilation (crack initiation stress); I: determined from the volumetric strain response according to Brace et al. (1966); II: determined from the radial strain response according to Lajtai (1974)

were used to show the influence of mineralogical composition on UCS and σ_{CI} as shown in Fig. 7a and b. Depending on the mass fraction of clay minerals, two distinctly different domains were identified (Fig. 7): a Domain I, where the clay content is <7 to 10 %, and a Domain II, where the clay content is greater. When the clay content exceeds 7–10 % (Domain II), σ_{CI} shows little scatter and is almost constant at 7 MPa (Fig. 7a). In the same domain, the unconfined compressive strength tends to decrease from approximately 20–5 MPa with increasing clay content (Fig. 7b). The data also suggest that the specimen geometry is of minor relevance for both the unconfined compressive strength and crack initiation threshold when the clay content is >20 % (Fig. 3).

For a clay mineral content <7–10 % (Domain I), both UCS and σ_{CI} increase substantially with decreasing clay content (Fig. 7a, b), thus increasing anhydrite and Dolomite content. In Domain I, the UCS and σ_{CI} decrease in an almost linear manner, even though the scatter is high at the transition between the two domains.

3.1.3 *Influence of Microstructural Variations and Rock Fabric on σ_{CI} and UCS*

A series of thin sections obtained from representative specimens utilized for unconfined compressive strength tests was analyzed to investigate variations in σ_{CI} and UCS associated with microstructural and mineralogical

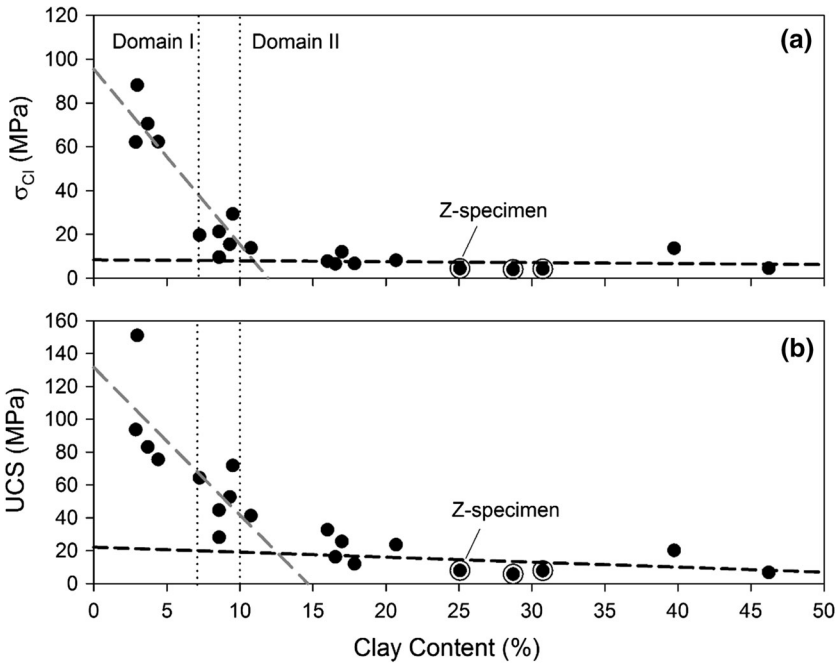

Fig. 7 Relationships between total content of clay minerals and **a** crack initiation stress (σ_{CI}), and **b** unconfined compressive strength (UCS); Z-specimens are shown with *double circle*. The crack initiation data shown in **a** were determined according to Method I (Brace et al. 1966)

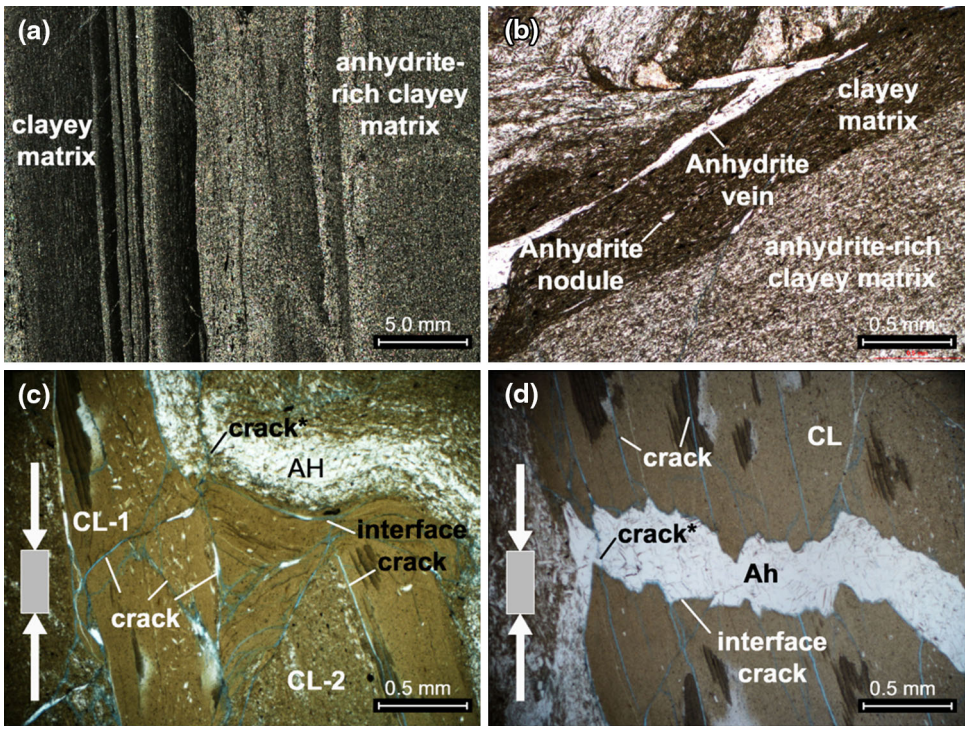

Fig. 8 Results of the thin section analyses. The thin sections in **a** and **b** were prepared from specimens before mechanical testing. The thin sections in **c** and **d** were prepared from specimens after mechanical testing (unconfined compression tests). The specimens are representative for Domain II and the transition between Domain I and II (Fig. 7). The load axis is indicated by *arrows*. *Ah* Anhydrite, *CL* Clayey matrix, *crack** crack which penetrates Anhydrite veins or anhydrite-rich zone. *CL-1* and *CL-2* indicate microstructural and mineralogical variations in the clayey matrix. *CL-2* is characterized by continuous distributed anhydrite; the anhydrite content is therefore higher than in *CL-1*

variations of the clayey matrix. Thin sections in Fig. 8a and b are representative for specimen in Domain II, and the transition zone between Domains I and II. Macroscopically, the fabric of these specimens is characterized by distinct heterogeneities within a (macroscopically) homogeneous clayey matrix. Heterogeneities such as layers, veins or nodules on the mm- to cm-scale are typically made up of polycrystalline anhydrite. The microscopic analyses of the clayey matrix revealed, however, distinct differences in the microstructure and mineralogical composition of the clayey matrix. The dark gray to almost black clayey matrix in Fig. 8a and b predominately consists of clay minerals with spatially distributed fine-grained anhydrite nodules or veins (white) on the sub-mm scale. The light gray matrix type in Fig. 8a and b is made of fine-grained clay and homogeneously distributed fine-grained anhydrite minerals

(called anhydrite-rich matrix). In general, the anhydrite content and distribution in the clayey matrix vary, and different matrix types usually co-exist in one specimen.

Klinkenberg et al. (2009) reported similar observations for other rock types. They analyzed the influence of the microstructure and mineralogical composition on the strength of Tournemire Shale, and showed that carbonate was homogeneously distributed in the clayey matrix. With increasing carbonate content, the strength of this shale increased. Klinkenberg et al. (2009) concluded that the increase in strength of the shale is associated with an increasing strength of the clayey matrix when the carbonate content increases. Based on these observations and the findings of Klinkenberg et al. (2009), it is suggested here that variations in the magnitude of σ_{CI} are related to microstructural and mineralogical differences of the clayey matrix. In Domain II, a little scatter in σ_{CI} indicates that the differential stress required to initiate microcracks is almost constant. The increase of σ_{CI} in Domain I is interpreted to be related to an increasing anhydrite content within the clayey matrix and thus strength of the clayey matrix. The occurrence of different clayey matrix types and the transition to clayey matrix types with increasing anhydrite content in Domain I might also explain the variability in σ_{CI} in the transition zone between Domains I and II. Specimens which contain a few zones with lower strength clayey matrix sandwiched between a predominately higher strength clayey matrix (anhydrite-rich matrix) can show a low σ_{CI} value, although the total content of anhydrite is relatively high.

A general increase in matrix strength with increasing anhydrite content (and decreasing clay content) might also explain the increase in UCS in Domain I.

As outlined in the previous section, σ_{CI} of specimens with an unconfined compressive strength larger than approximately 75 MPa (H-specimens) increases slightly at a rate of 3:10 (Fig. 6). These specimens show a substantially different fabric compared to specimens in Domain II and the transition zone. Distinct layers of clay rock cannot be found and the specimens appear macroscopically homogeneous (Fig. 9); though, the mineralogical analyses revealed clay content up to 5 % (Table 2). The stress at the onset of dilation for these specimens therefore represents a threshold of an almost homogeneous anhydrite rather than a property which represents the strength or strength variability of a clayey matrix.

3.1.4 Failure Process Observed During Unconfined Compression Tests

The analysis of the failure processes is based on a series of thin sections prepared after mechanical perturbation. Only specimens exceeding 5 % clay mineral content and a strength <80 MPa were utilized. As mentioned above, these specimens show a fabric which is characterized by a clayey matrix with distinct heterogeneities (e.g., layers) on the mm- to cm-scale. This rock fabric is representative for the conditions encountered in the six boreholes (Fig. 10). Note that also a series of thin sections was prepared before mechanical loading. These thin sections showed no microcracks, which indicate that the observed microcracks are solely associated with deviatoric loading in the laboratory.

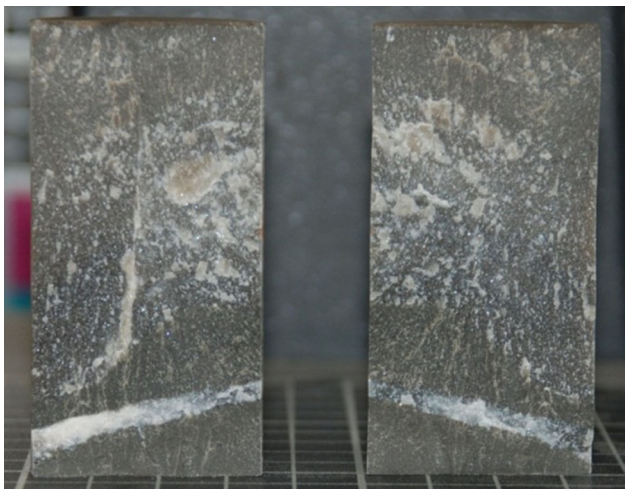

Fig. 9 Fabric of a typical specimen in Domain I where the clay mineral content is <5 %. No distinct layers of clay rock can be observed

Figure 8c and d shows typical thin sections with several microcracks in the clayey matrix. The microcracks are often oriented sub-parallel to the principal load direction (as indicated by arrows in Fig. 8c, d) and tend to open normal to the plane of the cracks. It was also observed, for example in Fig. 8c, that the orientation of microcracks is variable and often oblique to the loading axis, probably due to microstructural or mineralogical variations (e.g., preferred orientation of clay minerals or distribution and mass fraction of fine-grained anhydrite). As shown in Fig. 8c and d, microcracks get arrested at the interface between clay rock and heterogeneities such as anhydrite layers, veins or nodules. Figure 8c and d also shows microcracks alongside the interface between the clay matrix and the heterogeneity (called interface cracks). Interface cracks typically form alongside the anhydrite veins or nodules (Fig. 8d) or, as shown in Fig. 8c, alongside the anhydrite-rich clayey matrix zones. The latter observation supports that the anhydrite-rich clayey matrix has a higher strength and stiffness than the clay-rich matrix. The analyses of several thin sections revealed that the majority of the observed microcracks are distributed in the clayey matrix or follow an interface between the clayey matrix and heterogeneities. Interface cracks often link with micro-cracked clay layer. Microcracks may also penetrate stiff heterogeneities such

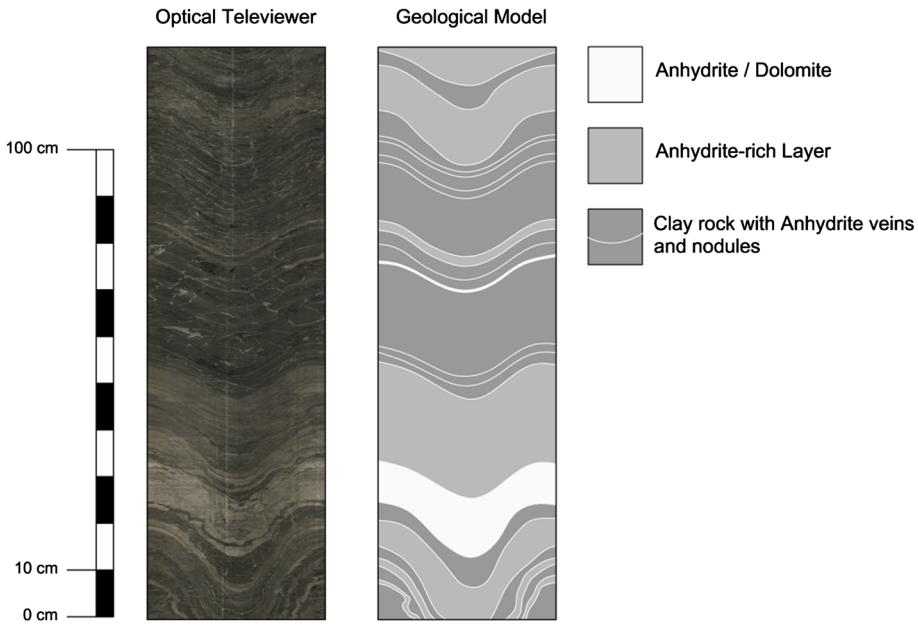

Fig. 10 Typical appearance of the Gipskeuper formation encountered in the six boreholes (location shown in Fig. 2). The *left* figure shows a section of the unwrapped optical televiewer image obtained in BH 4. The *right* figure shows the geological model

as anhydrite as shown in Fig. 8c and d. Such microcracks typically link micro-fractured clayey layers where the fabric of the rock prevents linking through interface cracks, or when a clay nodule is surrounded by anhydrite. Since heterogeneities are typically stiffer and stronger than the clayey matrix, it is assumed that microcracks penetrating stiff heterogeneities may have formed at higher axial stress levels than interface cracks.

As mentioned above, microcracks in the clayey matrix often tend to open normal to the principal load direction. Under laterally unconfined conditions, this process is associated with an increase in the radial strain. Figure 11 shows the relationship between the axial and the radial strain in the pre-failure region for a typical, heterogeneous specimen as the axial stress is increased. At low axial strain, the curve corresponds to an elastic response, following the Poisson's effect. However, with increasing axial strain, at about 0.04 % in this case, the radial strain increases disproportionately to the axial strain, indicating an ever increasing growth of extensional axial cracks. This disproportional increase often leads to an extensional macroscopic fracture (defined as fractures with a length on the cm-scale which are visible by naked eye) aligned with the maximum principal stress axis. Under laterally unconfined conditions, such macroscopic axial fractures are usually visible in brittle rock types when the axial stress exceeds the crack damage threshold where a critical crack density is reached (Fig. 1; Bieniawski 1967; Martin 1997). However, it was observed in this study that, for heterogeneous sulfate-rich rocks, the majority of specimens do not show macroscopic cracks prior to or at failure (peak strength). Some specimens did not show macroscopic fractures even after intense post-

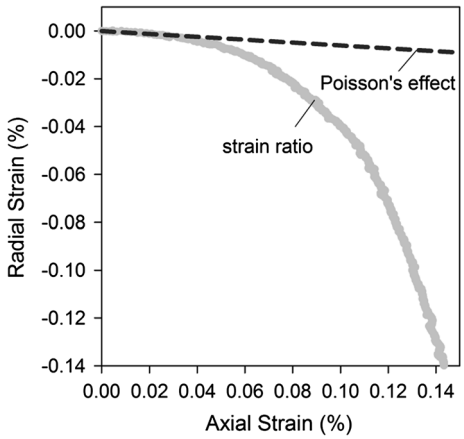

Fig. 11 Ratio between axial strain and radial strain typically observed in the pre-failure range during unconfined compression tests (specimen no. B3 318 is shown here) on specimens with a heterogeneous rock fabric (Domain II, and transition between Domains I and II)

failure straining (to as much as −0.5 % radial strain). Only specimens with a homogeneous fabric (clay content <5 %; Fig. 9) showed macroscopic cracks prior to failure. This observation, together with the observations from microscopic investigation, suggests that microcracks forming under unconfined compression in heterogeneous specimens do not localize or form a macroscopic fracture prior to failure. This process is most probably controlled by the quantity, orientation and distribution of anhydrite veins which tend to arrest growing microcracks. Unstable crack growth in the pre-failure range, as typically observed in other brittle rock types (Bieniawski 1967; Martin 1997), may therefore be less probable in specimens with a

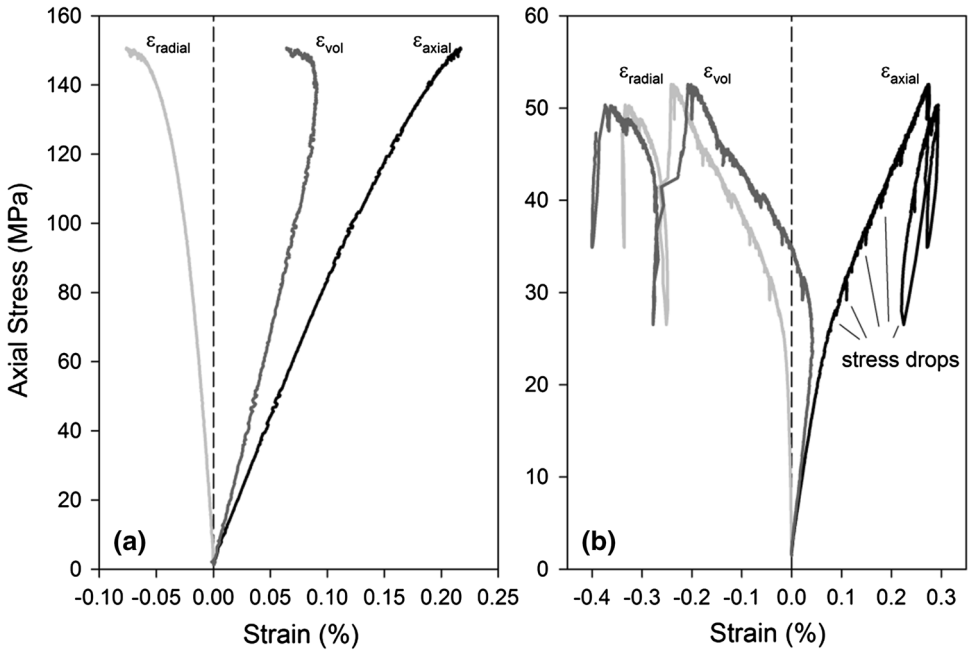

Fig. 12 Stress–strain response typical for specimen with **a** homogeneous rock fabric (Domain I) and **b** heterogeneous rock fabric with distinct clay layers and stiff heterogeneities (Domain II, and transition between Domain I and II)

heterogeneous rock fabric with considerable stiffness or strength heterogeneities.

The heterogeneous rock fabric and microstructure may also explain the sudden, distinct stress drops observed at different axial stress levels (Fig. 12b). Note that a constant circumferential displacement rate was utilized as the controlling feedback signal for these unconfined compression tests. Therefore, stress drops are associated with the tendency of a sudden increase of the circumferential displacement rate as a consequence of microcrack initiation or propagation. Figure 12 shows the stress–strain behavior representative for specimens in Domain I and the transition zone between Domain I and II (Fig. 7). Specimens in Domain I, with no discrete clay layers (H-specimen), do not show considerable stress drops, whereas specimen in the transition zone (and in Domain II) characterized by a rock fabric consisting of distinct layers of clay rock with stiff heterogeneities, exhibited several considerable stress drops of various magnitudes in the pre-peak and post-peak region (Fig. 12b). As outlined in the previous section, different clay matrix types co-exist in a specimen. Each stress drop is interpreted as an indication of cracking of spatially distributed clayey matrix zones with different strength properties. In addition to the variability in the strength of the clayey matrix, it is reasonable to assume that the heterogeneous rock fabric creates stress and strain heterogeneities. As a consequence, the stress or strain threshold required to initiate microcracks is eventually exceeded locally while other regions of the specimens still respond elastically to loading. Stiff heterogeneities may also experience less straining compared to clay layers were micro-fracturing is initiated at lower stress levels. The resulting strain differential can induce shear or tensile stresses at the interfaces, and ultimately lead to the formation of interface cracks as shown in Fig. 8. Sudden stress drops at higher stress levels could also be related to cracking of stiff heterogeneities or interface cracks. In the post-peak range, these stress drops are often considerably larger as shown in Fig. 12b. It is assumed that the majority of these stress drops are associated with s penetrating anhydrite veins or the formation of larger interface cracks.

In this study, the axial strain obtained from heterogeneous specimens (Domain I and transition zone between Domains I and II) typically deviated from linearity at axial stresses below the crack damage threshold but above σ_{CI} as illustrated in Fig. 12b. The axial strain for a typical brittle rock is, however, linear until the threshold stress for unstable crack growth at σ_{CD} (coalescence of distributed microcracks) is reached (Fig. 1; Bieniawski 1967). This is because the majority of distributed microcracks are true Mode I cracks that grow sub-parallel with the maximum far-field stress, and thus should not affect the axial strain as they form during the initial brittle damage phase (Bieniawski 1967). A deviation of the stress-axial strain curve from linearity at stress levels below σ_{CD} (but above σ_{CI}) was reported by Eberhardt et al. (1998) for laterally unconfined tests on Lac du Bonnet Granite. They suggested that prior to the onset of unstable crack growth at σ_{CD}, coalescence of individual cracks occurred involving some microcrack growth at oblique angles to the loading direction, accompanied by some shearing. As shown in the previous section, interface cracks are often oblique to the principal load direction and eventually link micro-fractured clay layers in the specimen. Thus, the deviation from

Table 3 Results of the triaxial tests

Borehole	Depth (cm)	Specimen	D (mm)	E (GPa)	υ	σ_3 (MPa)	$\sigma_{1,peak}$ (MPa)	$\sigma_{CI,AE}$ (MPa)	$\sigma_{CI,vol}$ (MPa)
B4	330	Z	34	14.5	0.14	8	71.5	15.0	13.9
B1	270	Z	34	12.1	0.30	2	39.9	8.2	8.3
B3	249	Z	34	24.2	0.10	2	46.9	8.4	9.5
B4	267	Z	34	5.4	0.31	1	44.7	8.6	–
B4	335	Z	34	22.3	0.37	1	31	6.2	–
B4	335	Z	34	10.1	0.30	2	42	6.1	6.5
B4	405	P	34	11.2	0.20	8	53.7	15.6	16.2
B3	440	P	34	12.3	0.07	2	43.2	-	7.7
B4	275	P[a]	34	25.8	0.08	8	101	15.7	15.8
B3	455	F	34	29.9	0.31	8	93.8	14.5	16.6
B3	245	P[a]	34	25.8	0.27	1	67.3	7.1	7.3
B3	231	F	34	32.1	0.10	4	89.8	10.5	11.6
B3	227	P	34	37.4	0.16	4	112	11.9	12.0
B5	505	P	34	64.9	0.19	2	116.3	9.6	10.0
B4	495	P	34	62	0.10	1	99	–	–

Z Z-specimen, *P* P-specimen, *F* F-specimen, *D* specimen diameter, *E* Young's Modulus, υ Poisson's value, σ_3 confining stress, $\sigma_{1,peak}$ peak strength, $\sigma_{CI,AE}$ axial stress at crack initiation obtained from acoustic emission monitoring, $\sigma_{CI,vol}$ axial stress at crack initiation obtained from volumetric strain response according to Brace et al. (1966)

[a] P-specimens with discontinuous stiff layers

linearity of the axial strain curve is interpreted as indicating the formation of inclined fractures in the specimen similar to those shown in Fig. 8c, and the activation of shearing on oblique cracks.

From the discussion above it is evident that for specimens with a heterogeneous rock fabric the likelihood for growing microcracks to arrest at anhydrite veins is associated with their total amount, orientation and distribution. At high clay content (and with low density of anhydrite veins) the possibility to form a macroscopic fracture is higher compared to a specimen with a high density of anhydrite veins. With increasing density of anhydrite veins, therefore, individual cracks or micro-fractured zones cannot coalescence at low axial loads, and fractures ultimately have to propagate through heterogeneities. This may explain the increase in peak strength with decreasing clay content or increasing mass fraction of anhydrite. Thus, specimens with a weak clayey matrix but a high content of stiff heterogeneities may show a low crack initiation stress but a high strength due to a high density of anhydrite veins.

3.2 Confined Compressive Strength Tests

Confined (triaxial) compressive strength tests were performed on specimens with a heterogeneous fabric (i.e., fabric with distinct layers of clay rock and stiff heterogeneities). The results obtained from 15 triaxial tests are summarized in Table 3. The results of the mineralogical analyses of the specimens are listed in Table 4. The clay content for these triaxial specimen ranges between 6.7 and 33.8 %, and thus the specimens belong to Domain II and the transition between Domain I and II (Fig. 7).

3.2.1 *Onset of Dilation in Confined Compression Tests*

Figure 13 shows the onset of micro-cracking (dilation) at σ_{CI} under triaxial compression in a principal stress (Fig. 13a) and differential stress diagram (Fig. 13b). Both, crack initiation obtained from micro-acoustic emission monitoring and the volumetric strain response are shown. It can be seen that with increasing confining stress the axial stress at σ_{CI} tends to slightly increase with a slope of 1.15. The differential stress at σ_{CI} is, however, almost independent of the confinement (Fig. 13b; slope of 0.15), and ranges between 4 and 8 MPa. Furthermore, the differential stress at crack initiation obtained from Z-specimens (six out of 15 specimens; Table 1) is approximately equal to crack initiation stress values obtained from P- and F-Specimens suggesting that the load direction in respect to the bedding plane orientation is of minor relevance when the clay content exceeds 7 %. The differential stress required to initiate microcracks is consistent with σ_{CI} values obtained from unconfined compression test on specimens with a clay content exceeding 7–10 % for which σ_{CI} ranges between 4 and 13 MPa.

The independency of the differential stress at σ_{CI} from the confining stress suggests that friction is not or only

Table 4 Results obtained from XRD analyses on specimens used for triaxial compressive strength tests

Borehole	Depth (m)	Ah (%)	Gy (%)	Ba (%)	Do (%)	Q (%)	Mg (%)	CM (%)
B4	330	76.0	0	0	0	2.7	5.8	10.94
B1	270	78.72	0.26	1.09	0.2	2.17	18.85	9.33
B3	249	54.4	0	1.23	0	6.35	13.57	13.72
B4	267	67.0	0.34	1.3	0	5.31	10.85	9.21
B4	335	63.1	1.34	0.52	0	5.67	7.01	13.31
B4	335	63.1	1.34	0.52	0	5.67	7.01	13.31
B4	405	27.1	0	3.9	0	7.01	20.09	33.81
B3	440	54.4	0	0	0	4.06	13.71	20.4
B4	275	67.0	0.34	1.3	0	5.31	10.85	9.21
B3	455	70.3	0	1.48	0	2.45	8.81	11.49
B3	245	70.15	0.31	1.51	0.04	2.61	10.12	9.36
B3	231	55.5	0.43	1.1	0	6	18.71	9.87
B3	227	56.5	0.22	1.24	0	4.83	23.54	7.23
B5	505	71.4	0	0.17	0	5.07	13.32	6.7
B4	495	68.8	0.78	1.52	0	4.51	11.39	6.84

Ah anhydrite, *Gy* gypsum, *Ba* bassanite, *Do* dolomite, *Q* quartz, *Mg* magnesite, *CM* clay minerals (e.g., sum of smectite illite, chlorite)

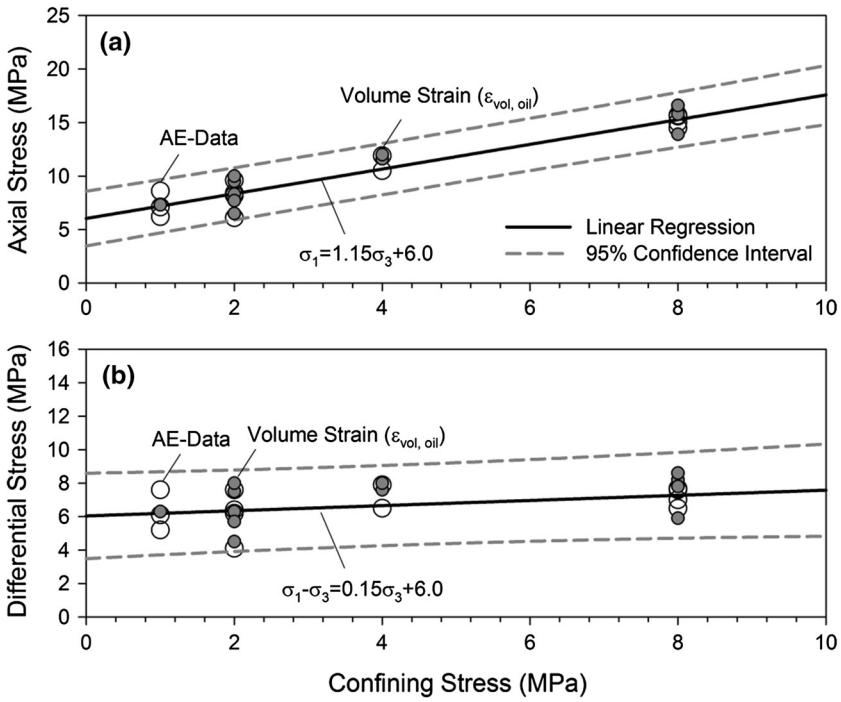

Fig. 13 Stresses at the onset of dilatancy in triaxial compression: **a** principal stress diagram; **b** differential stress versus confining stress. Both crack initiation obtained from micro-acoustic emission (AE) monitoring (*open circles*) and the volumetric strain response ($\varepsilon_{vol, oil}$) (*filled circles*) are shown

marginally mobilized at this stage of rock fracturing process. A linear least-square regression analyses revealed a friction angle of only 4°. Similar findings have been obtained by Amann et al. (2011b) from triaxial compressive strength tests on over-consolidated clay rock (Opalinus Clay). They showed that the differential stress at the onset of dilation was independent of confinement which suggests that no friction is mobilized at the crack initiation stage of the brittle failure process.

3.2.2 *Failure Processes During Confined Compressive Loading*

Acoustic emission data recorded during several triaxial tests revealed a step-wise increase in acoustic emission counts with increasing differential stress, rather than a continuous increase as typically observed on other brittle rock types (Eberhardt et al. 1998; Mogi 1962). This is illustrated by Fig. 14 showing at least five steps and

plateaus at different differential stress levels. The reasons for the step-wise increase in acoustic emissions with increasing differential loading are interpreted as being related to the same reasons described earlier when discussing the observed stress drops in the pre-peak region of unconfined compression tests. Variations in the strength of the clayey matrix due to mineralogical or microstructural variations, and stress or strain heterogeneities are seen as the cause for local clay matrix cracking or failure.

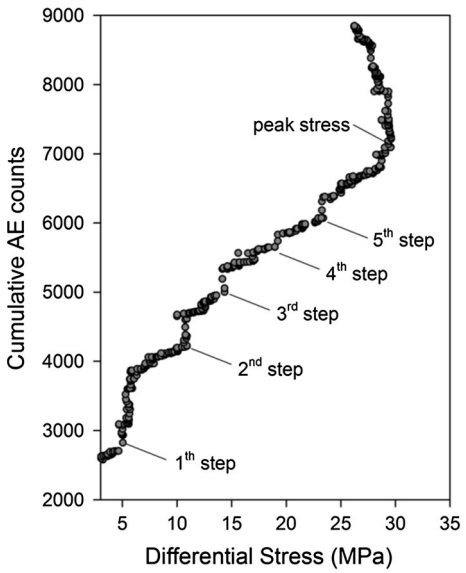

Fig. 14 Discontinuous step-wise increase of acoustic emission events often observed during triaxial compression tests on specimens with a heterogeneous rock fabric

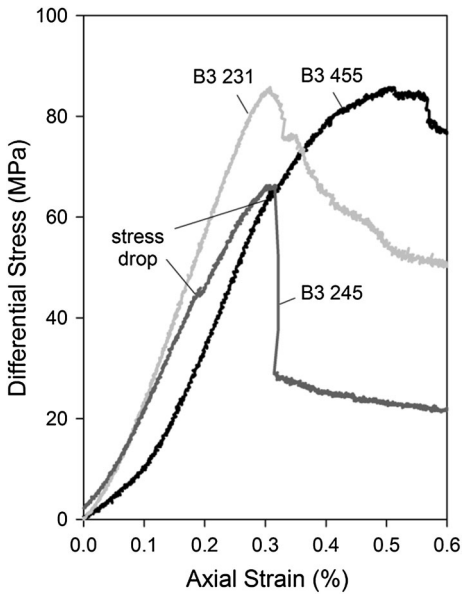

Fig. 15 Stress–axial strain response of selected triaxial specimens. Distinct stress drops can be seen in the stress–axial strain response of specimen B3 455 and B3 245

However, major stress drops in the pre-peak region were rarely observed in the stress–strain response obtained from triaxial tests (Fig. 15; two of the three cases show a distinct stress drop in the pre-failure region). In addition, the majority of stress drops observed during triaxial compression tests occurred when the confining stress was low (e.g., $\leq$2 MPa confinement). At higher confining stresses stress drops were rarely observed for tests on F- and P-specimens (e.g., specimen B 3 455; Fig. 15), but systematically on Z-specimens.

The difference in stress drop frequency in the pre-failure range between unconfined and confined compression tests is most likely associated with the different types of loading used. Confined test were run with constant axial displacement rate, and the axial load increased steadily throughout the loading. In contrast, unconfined tests were run with constant circumferential displacement rate. For the latter, distinct stress drops are associated with the tendency of sudden changes in radial displacement due to the growth of extensional axial microcracks. This suggests that stress drops observed in unconfined compression tests are predominately associated with extensional fractures which are aligned with the principal load axis. Stress drops during axial displacement-controlled triaxial tests might indicate the formation or activation of shearing along oblique fractures as discussed in the previous section.

3.2.3 Failure Envelope

The analyses of unconfined compressive strength data showed that the rock strength primarily depends on the mass fraction of clay minerals and the distribution and orientation of anhydrite veins. For clay content >20 %, the specimen geometry is of minor relevance in terms of strength. Specimens utilized for triaxial tests covered clay mineral content between 6.7 and 33.8 %, and the peak strength values, as illustrated in Fig. 16, consequently show considerable scatter. Depending on the mineralogical composition and failure mechanism (i.e., with failure predominantly through the clayey matrix), three groups with similar mineralogical composition, strength and failure characteristics could be identified (Fig. 16). For the first group (Group I), results obtained from Z-specimen are combined with results from specimens with a clay content >20 %, where specimen failure is controlled by the clayey matrix. Results from unconfined compressive strength tests on specimens which failed along a discrete bedding plane without involving intact rock fracturing showed exceptional low strength and were not considered. Specimens in the second group (Group II) are characterized by clay content between 8.5 and 11.5 % and folded (F-specimen) or discontinuous layers of stiff heterogeneities oriented parallel to the loading axis (P-Specimen with discontinuous

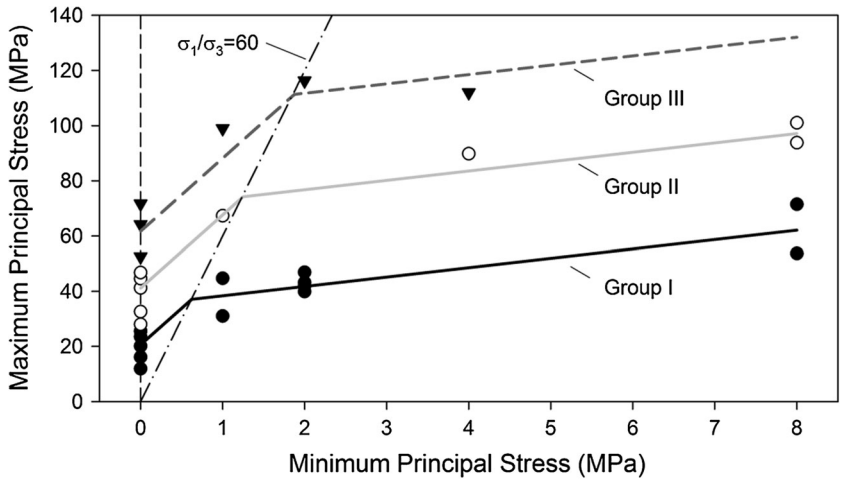

Fig. 16 Peak strength data obtained from unconfined and confined compression tests

stiff heterogeneities). Specimens in the third group (Group III) have clay content between 6.7 and 9.5 % and continuous anhydrite layers oriented parallel to the load axis (P-specimen).

The data points shown in Fig. 16 suggest that the peak strength cannot adequately be described by a linear failure envelope. A bilinear envelope was used to account for the rapid strength gain at lower confining stress. The amount of data obtained in this study is insufficient to establish a peak failure envelope for the three groups by statistical means. However, a peak strength failure envelope was established for the three groups by assuming that the friction angle (or slope in the principal stress diagram) of all specimen groups is the same in the lower and the higher confining stress range. Data obtained from Z-specimens and specimens with high clay content at a confining stress range >1 MPa were used to estimate the friction angle for the higher confining stresses by least-square linear regression. The friction angle obtained is 33°. The effective friction angle (friction plus dilation angle) for lower confining stresses was established from Group II and Group III and revealed a consistent value of 68° (interpreted as 33° friction angle plus 35° dilation angle). Figure 16 shows the three bilinear failure envelopes for the three specimen types, assuming that the friction at high confinement (beyond the spalling limit $\sigma_1/\sigma_3 = 60$) is the same for all specimens groups.

4 Practical Implications for Tunelling

The rock mass strength in the low-confinement zone around tunnels in massive to moderately jointed brittle rock is often substantially lower than that predicted from laboratory tests (Martin 1997; Diederichs 2003). It has been shown that the stress required to initiate macroscopic fractures in this low-confinement zone is approximately equal to the crack initiation threshold obtained from compressive strength tests (Martin 1997; Diederichs 2003). In other words, slight stress increases beyond the crack initiation threshold can lead to spalling. However, sulfate-rich clay rocks contain stiff heterogeneities at various scales (Figs. 8, 10). For example, in folded and layered Gipskeuper formations, several distinct layers, predominately made of anhydrite, may be encountered. The thickness of these layers is typically on the centimeter to decimeter scale, and the majority of the rock mass consists of a sequence of clay rock with varying clay content, and spatially distributed veins or nodules (predominantly anhydrite) with a thickness on the mm-scale. The experimental findings from this study suggest that crack initiation in this heterogeneous rock type may not be synonymous with crack propagation leading to spalling and rock mass disintegration, because stiff heterogeneities may arrest propagating fractures and thus prevent rock mass disintegration. As a consequence, the self-supporting capacity of the damaged rock mass may be maintained, rendering instability problems such as raveling less likely.

Furthermore, as suggested by Alonso and Berdugo (2006), fissures and cracks in a damage zone around a tunnel may promote swelling by crystal growth when sulfate-rich groundwater approaches and becomes supersaturated. The analysis on sulfate-rich clay rocks in this study shows that micro-fracturing may occur around tunnels at low differential stress levels, which might increase the potential for gypsum precipitation.

5 Conclusion

A series of unconfined and confined compression tests with acoustic emission monitoring was used in combination

with mineralogical and microstructural analyses to investigate the failure behavior of sulfate-rich clay rocks. This study of rock specimens obtained from the Belchen Drainage Tunnel in Switzerland suggests that microcracks in the clayey matrix are first initiated at a differential stress ranging between 4 and 13 MPa. For specimens with a clay content >7 %, the differential stress at crack initiation is independent of the specimen geometry and the confining stress. Microstructural and mineralogical variations are seen as the primary cause of strength and stiffness variations in the clayey matrix. Upon compressive loading, these heterogeneities may cause stress or strain heterogeneities and, as a consequence, localized failure processes at different strain or stress levels. This is supported by sudden stress drops systematically observed in the stress–strain response obtained from unconfined compression tests, and the step-wise increase in acoustic emission counts during confined compression tests.

At the specimen scale, it was shown that microcracks are initiated at low differential stresses, but crack propagation is often hindered by anhydrite veins. These veins may prevent unstable crack growth. Depending on the orientation, distribution and mass fraction of stiff heterogeneities, specimen failure requires high stresses or strains to link micro-fractured region either by interface cracks or by cracks which penetrate anhydrite veins.

The crack initiation threshold which occurs at low deviatoric stresses is therefore a property of the clayey matrix, while the strength of the specimen primarily depends on the fabric (e.g., amount, orientation and distribution of stiff heterogeneities). The inferred ratio between crack initiation stress and peak stress, as typically used to quantify the onset of the failure process of brittle rock types, is therefore misleading for this type of rock. This is due to the fact that the peak strength of a specimen with a high anhydrite vein density can be relatively high, while the strength of the clayey matrix is exceeded at low stresses.

Sulfate-rich clay rocks typically contain anhydrite veins at various scales. At the scale of a tunnel, anhydrite layers or veins may arrest growing fractures and prevent the disintegration of the rock mass. The rock mass may be damaged when the threshold stress for microcrack initiation is exceeded, but the self-supporting capacity of the rock mass may be maintained rendering the possibility for rapidly propagating instability less likely.

Acknowledgments This study was funded by the Swiss Federal Road Office ASTRA (project ASTRA 2011_006). We are grateful to Dr. M. Plötze (Institute of Geotechnical Engineering, Swiss Federal Institute of Technology) for his advice and equipment to perform the XRD analyses for this study, and Dr. Walter Steiner for fruitful discussions.

References

Alonso E, Berdugo IR (2006) Degradation and swelling of sulphate-bearing claystones. In: Montero JM, Colmenares JE (eds) Paper presented at VI CSAMR 2006, Cartanga, Colombia, pp 211–248

Amann F, Kaiser PK, Steiner W (2010) Triggering swelling potential of anhydrite clay rocks by brittle failure processes. In: Zhao J, Labious V, Dudt JP, Mathier JF (eds) Paper presented at European rock mechanics symposium 2010, Lausanne, Switzerland, Rock Mechanics and Environmental Engineering. Taylor and Francis Group, London, pp 339–342. ISBN 978-0-415-58654-2

Amann F, Button EA, Evans KF, Gischig VS, Blümel M (2011a) Experimental study of the brittle behavior of clay shale in short-term unconfined compression. Rock Mech Rock Eng 44(4):415–430

Amann F, Kaiser PK, Button EA (2011b) Experimental study of the brittle behavior of clay shale in rapid confined compression. Rock Mech Rock Eng 44(1):21–33

Amstad Ch, Kovari K (2001) Untertagbau in quellfähigem Fels, Eidgenössisches Department für Umwelt, Verkehr, Energie und Kommunikation (UVEK) & Bundesamt für Strassen (ASTRA), Zürich

Bieniawski ZT (1967) Mechanism of brittle failure of rock Part I—Theory of fracture process. Int J Rock Mech Min Sci Geomech Abstr 4(4):395–406

Brace WF, Paulding BR, Scholz C (1966) Dilatancy in fracture of crystalline rocks. J Geophys Res 71(16):3939–3953

Diederichs MS (2003) Rock fracture and collapse under low confinement conditions. Rock Mech Rock Eng 36(5):339–381

Eberhardt E, Stead D, Stimpson B, Read RS (1998) Identifying crack initiation and propagation thresholds in brittle rock. Can Geotech J 35:222–233

Fairhurst C, Cook NGW (1966) The phenomenon of rock splitting parallel to the direction of maximum compression in the neighborhood of a surface. In: Proceedings 1th congress of the international society of rock mechanics, Lisbon, pp 687–692

Hallbauer DK, Wagner H, Cook NGW (1973) Some observation concerning the microscopic and mechanical behaviour of quartzite specimens in stiff, triaxial compression tests. Int J Rock Mech Min Sci Geomech Abst 10:713–726

ISRM (1979) Suggested methods for determining the uniaxial compressive strength and deformability of rock materials. Int J Rock Mech Min Sci Geomech Abst 16(2):135–140

Kaiser PK, Kim BH (2008) Rock mechanics challenges in underground construction and mining. In: Potvin Y, Carter J, Dyskin A, Jeffery R (eds) Paper presented at 1th Sou. Hem. Int. Rock Mech. Sym., Australia, pp 23–38

Klinkenberg M, Kaufhold S, Dohrmann R, Siegesmund S (2009) Influence of carbonate micofabric on the failure strength of claystones. Eng Geol 107:42–54

Lajtai EZ (1974) Brittle fracture in compression. Int J Fract 10(4):525–536

Lockner DA, Moore DE, Reches Z (1992) Microcrack interaction leading to shear fracture, presented at the 33rd U.S. Rock Mechanics Symposium, edited by Tillerson and Wawersik, 908–816, Balkema, Rotterdam, 807-816

Martin CD (1997) Seventeenth Canadian Geotechnical Colloquium: the effects of cohesion loss and stress path on brittle rock strength. Can Geotech J 34:698–725

Martin CD, Chandler NA (1994) The progressive fracture of Lac du Bonnet granite. Int J Rock Mech Min Sci 31:643–659

Mogi K (1962) Study of elastic shocks caused by the fracture of heterogeneous materials and its relations to earthquake phenomena. Bull Earthq Res Inst 40:125–173

Nicksiar M, Martin CD (2012) Evaluation of methods for determining crack initiation in compression tests on low-porosity rocks. Rock Mech Rock Eng 45(4):607–617

Scholz CH (1968) Experimental study of the fracturing process in brittle rock. J Geophys Res 73(4):1447–1454

Steiner W (1993) Swelling rock in tunnels: characterization, effect of horizontal stresses and construction procedure. Int J Rock Mech Min Sci Geomech Abstr 30(4):361–380

Steiner W, Kaiser PK, Spaun G (2010) Role of brittle fracture on swelling behavior of weak rock tunnels: hypothesis and qualitative evidence. Geomech Tunn 3(5):583–596

Steiner W, Kaiser PK, Spaun G (2011) Role of brittle fracture on swelling behavior of weak rock tunnels: evidence from tunnelling case histories. Geomech Tunn 4(2):141–156

Tapponier P, Brace WF (1976) Development of stress-induced microcracks in Westerly Granit. Int J Rock Mech Min Sci 13:103–112

Vögtli B, Jordan P (1996) Quelldruckentwicklung in Ton- und Sulfatgesteinen. Schweizer Ingenieur und Architekt 18:16–180